The Spectral Correlation Function of Molecular Clouds: A Statistical Test for Theoretical Models

Paolo Padoan[1]
Jet Propulsion Laboratory, 4800 Oak Grove Drive, MS 169-506, California Institute of Technology, Pasadena, CA 91109-8099, USA

Alyssa A. Goodman
Harvard University Department of Astronomy, Cambridge, MA 02138

and Mika Juvela
Helsinki University Observatory, Tähtitorninmäki, P.O.Box 14, SF-00014 University of Helsinki, Finland

Received _____; accepted _____

[1]padoan@jpl.nasa.gov

ABSTRACT

We compute the spectral correlation function (SCF) of ^{13}CO J=1–0 maps of molecular cloud complexes. The SCF is a power law over approximately an order of magnitude in spatial separation in every map. The power law slope of the SCF, α, its normalization, S_0(1pc), and the spectral line width averaged over the whole map, σ_v, are computed for all the observational maps. The values of α , S_0(1pc) and σ_v are combined to obtain empirical correlations to be used as tests for theoretical models of molecular clouds. Synthetic spectral maps are computed from different theoretical models, including solutions of the magneto-hydrodynamic (MHD) equations with different values of the rms Mach number of the flow and stochastic models with different power spectra of the velocity field. In order to compute the radiative transfer from the MHD models it is necessary to assign the models a physical scale and a physical density. When these assignments are made according to Larson type relations the best fit to the observational correlations is obtained. Unphysical stochastic models are instead ruled out by the empirical correlations. MHD models with equipartition of magnetic and kinetic energy of turbulence do not reproduce the observational data when their average magnetic field is oriented approximately parallel to the line of sight.

Subject headings: turbulence – ISM: kinematics and dynamics – individual (Perseus, Taurus, Rosette); radio astronomy: interstellar: lines

1. Introduction

Molecular clouds are observed through the emission of a number of molecular transitions that provide a wealth of information about their chemical composition, gas temperature and density, magnetic field strength, fractional ionization, structure and kinematics. This information is essential to our understanding of the process of star formation.

The interpretation of molecular emission line maps is not always unique. The main source of uncertainty is the absence of the third spatial dimension (along the line of sight) in the observational data. Statistical properties of the velocity and density distributions along the line of sight are difficult to disentangle. Furthermore, the components of the gas velocity on the plane of the sky are unknown.

Two dimensional images of molecular clouds are usually converted into three dimensional "objects" using the radial velocity instead of the third spatial dimension. This method can be useful to separate individual mass condensations from each other, since it is conceivable that their relative velocity is larger than their internal one. However, velocity blending or the lack of well defined condensations along the line of sight may cause significant uncertainties. A number of authors have provided examples of plane–of–the–sky "clouds" that do not really exist as entities in three spatial dimensions (Ostriker, Stone & Gammie 2001; Lazarian et al. 2001).

Due to the difficulty of a direct interpretation of the observational data, a "forward approach" that starts from a rather general theoretical model and synthesizes its observational properties can be more instructive. Different models may sometimes satisfy the same set of observational constraints, but they should also provide guidance for further observational studies that could help select the correct model.

Ideally, numerical models to be compared with observed spectral line data cubes

should be based on the numerical solutions of the MHD equations, in the regime of highly super–sonic turbulence, and on radiative transfer calculations. In some works, stochastic fields are used instead of the solution of the MHD equations and in most studies the radiative transfer calculation is omitted, in favor of density–weighted velocity profiles. The first large synthetic spectral maps of molecular transitions computed by solving the non–LTE radiative transfer through the density and velocity data cubes obtained as the numerical solution of the MHD equations were presented by Padoan et al. (1998).

A number of statistical methods have been proposed to compare numerical models of turbulence with large spectral maps of molecular clouds (see for example Scalo 1984; Kleiner & Dickman 1985, 1987; Stutzki & Gusten 1990; Gill & Henriksen 1990; Houlahan & Scalo 1992; Hobson 1992; Langer, Wilson, & Anderson 1993; Williams, De Geus & Blitz 1994; Miesch & Bally 1994; Miesch & Scalo 1995; Lis et al. 1996; Blitz & Williams 1997; Heyer & Schloerb 1997; Stutzki et al. 1998; Miesch, Scalo & Bally 1999; Falgarone et al. 1994; Padoan et al. 1999; Mac Low & Ossenkopf 2000; Bensch, Stutzki & Ossenkopf 2001).

In this work we apply the spectral correlation function (SCF) method, proposed by Rosolowsky et al. (1999) and further developed in Padoan, Rosolowsky & Goodman (2001), to a number of observational and synthetic spectral maps. We show that the slope and normalization of the SCF of observational maps correlate with the spectral line width. Theoretical models of molecular clouds should therefore yield synthetic spectral maps reproducing such correlations, but not all of them can.

In the next section we briefly define the SCF, and in § 3 we present the observational data used in this work. The computation of the theoretical models and synthetic spectral maps is presented in § 4. Results are discussed in § 5 and conclusions drawn in § 6.

2. The SCF Method

The Spectral Correlation Function (SCF) measures the spatial correlation of spectral line profiles within a spectral map. It is sensitive to the properties of both the gas mass distribution and the gas velocity field (Rosolowsky et al. 1999; Padoan, Rosolowsky & Goodman 2001; Padoan et al. 2001).

Let $T(\mathbf{x}, v)$ be the antenna temperature as a function of velocity channel v at map position $\mathbf{x}$. The SCF for spectra with spatial separation ℓ is:

$$S_0(\ell) = \left\langle \frac{S_0(\mathbf{x}, \ell)}{S_{0,\mathrm{N}}(\mathbf{x})} \right\rangle_{\mathbf{x}}, \tag{1}$$

where the average is computed over all map positions $\mathbf{x}$. $S_0(\mathbf{x}, \ell)$ is the SCF uncorrected for the effects of noise,

$$S_0(\mathbf{x}, \ell) = \left\langle 1 - \sqrt{\frac{\Sigma_v [T(\mathbf{x}, v) - T(\mathbf{x} + \mathbf{\Delta x}, v)]^2}{\Sigma_v T(\mathbf{x}, v)^2 + \Sigma_v T(\mathbf{x} + \mathbf{\Delta x}, v)^2}} \right\rangle_{\mathbf{\Delta x}}, \tag{2}$$

where the average is limited to separation vectors $\mathbf{\Delta x}$ with $|\mathbf{\Delta x}| = \ell$, and $S_{0,\mathrm{N}}(\mathbf{x})$ is the SCF due to noise alone,

$$S_{0,\mathrm{N}}(\mathbf{x}) = 1 - \frac{1}{Q(\mathbf{x})}, \tag{3}$$

and $Q(\mathbf{x})$ is the "spectrum quality" (see discussion in Padoan, Rosolowsky & Goodman 2001). $Q(\mathbf{x})$ is defined as the ratio of the rms signal within a velocity window W and the rms noise, N (over all velocity channels),

$$Q(\mathbf{x}) = \frac{1}{N} \sqrt{\frac{\Sigma_v T(\mathbf{x}, v)^2 dv}{W}}, \tag{4}$$

where dv is the width of the velocity channels.

In the present work we compute the SCF of both observational and synthetic spectral maps, obtained by computing the radiative transfer through the three–dimensional density and velocity fields of numerical simulations of super–sonic MHD turbulence. The result

is typically a power law for $S_0(\ell)$ that extends up to a separation ℓ comparable to the map size, reflecting the self–similarity of super–sonic turbulence (Padoan, Rosolowsky & Goodman 2001). The power law behavior is sometimes interrupted at an intermediate scale, possibly suggesting the presence of a physical mechanism limiting the inertial range of turbulence. An example of a SCF that defines an intermediate scale is the SCF of the HI survey of the Large Magellanic Cloud (LMC) by Kim et al. (1998, 1999). Padoan et al. (2001) have recently been able to map the gas disk thickness of the LMC, assuming it is related to the intermediate scale defined by the break in the SCF power law.

3. The Observational Data

The absolute value of $S_0(\ell)$ at any ℓ and the slope of the $S_0(\ell)$ power law for any given region depends on which molecular tracer is used (Padoan, Rosolowsky & Goodman 2001). Transitions probing higher gas density produce more fragmented integrated intensity maps than transitions probing lower gas density, and their SCF is therefore steeper. In order to compare the SCF of observational and synthetic maps it is therefore important to solve the radiative transfer through the model density and velocity fields accurately for the same molecular transition that is observed.

In this work our aim is to compute the SCF of observational data in order to provide constraints for theoretical models. The best constraints come from computing the SCF of spectral maps of a specific molecular transition over a large range of line width and linear size. Observationally, small scale and narrow line width objects are usually mapped out with high density tracers, while larger objects are instead usually probed with lower density tracers. ^{13}CO provides a good compromise, since it is the only molecule for which very large maps containing thousands of spectra have been obtained with a significant range of resolution. In this work we have therefore chosen to use observational and synthetic maps

of the J=1–0 line of ^{13}CO.

We have used 11 ^{13}CO maps. For each map, we have listed in Table 1 the approximate size, the distance, the rms velocity computed as the standard deviation of the line profile averaged over the whole map, the telescope beam size, the spatial sampling, the width of the velocity channels and the spectral quality defined in the previous section. Smaller maps have been obtained from portions of the maps of the Taurus, Perseus and Rosette molecular cloud complexes and the SCF has been computed for each of them. The position of these smaller maps within the molecular cloud complexes is shown in Figures 1 and 2. They have been called T1 to T7 in Taurus, P1 to P5 in Perseus, R1B in the Rosette Molecular cloud map by Blitz & Stark (1986) and R1 and R2 in the Rosette Molecular cloud map by Heyer et al. (2001). [2]

The SCF of each map has been approximated with a power law, over the range of spatial separations where a power law fit is relevant. For each power law fit we compute its slope, α, and its absolute value at 1 pc, S_0(1pc):

$$S_0(\ell) = S_0(1\,pc)\left(\frac{\ell}{1\,pc}\right)^{-\alpha} \tag{5}$$

The values of α, S_0(1pc), σ_v (the line of sight rms velocity) and the galactic coordinates of the center of each map are given in Table 2. The SCF of maps of molecular cloud complexes and some smaller regions are shown in Figure 3.

4. MHD Simulations and Synthetic Spectral Maps

We solve the compressible MHD equations in a staggered mesh, with volume centered mass density and thermal energy, face centered velocity and magnetic field components,

[2]More conventional designations for some of the subregions are given in Table 2

edge centered electric currents and electric fields and with periodic boundary conditions. The code uses shock and current sheet capturing techniques to ensure that magnetic and viscous dissipation at the smallest resolved scales provide the necessary dissipation paths for magnetic and kinetic energy. A more detailed presentation of the numerical method can be found elsewhere. (Padoan & Nordlund 1999).

For the purpose of the present work we have computed numerical solutions of the MHD equations using an isothermal equation of state, and a random driving force. In all experiments, the initial density is uniform, and the initial velocity is random. We generate the velocity field in Fourier space, and we give power, with a normal distribution, only to the Fourier components in the shell of wave-numbers $1 \leq kL/2\pi \leq 2$. We perform a Helmholtz decomposition, and use only the solenoidal component of the initial velocity. However, a compressional component of the velocity field develops almost immediately due to the flow compressibility. The external driving force is generated on large scales in the same way as the velocity field. The initial magnetic field is uniform, and is oriented parallel to the z axis: $\mathbf{B} = B_0\hat{\mathbf{z}}$.

4.1. Numerical Models

We have run a number of MHD simulations in a 128^3 computational mesh, with periodic boundary conditions. The simulations are intended to describe the turbulent dynamics in the interior of molecular clouds. The two most important numerical parameters in the models are the rms sonic and Alfvénic Mach numbers, $M_{\rm S}$ and $M_{\rm A}$. The rms sonic Mach number is here defined as the ratio of the rms flow velocity and the speed of sound. The Alfvénic Mach number is defined as the ratio of the rms flow velocity and the Alfvén velocity, $v_{\rm A} = B/\sqrt{4\pi\rho}$, where B is the volume–averaged magnetic field strength.

All the models used in this work have $M_A = 10$, except for model E that has $M_A = 1$, according to the suggestion that the dynamics of molecular clouds is essentially super–Alfvénic (Padoan & Nordlund 1999). Our numerical simulations conserve magnetic flux, and so the volume averaged magnetic field is constant in time. As a consequence, also the value of M_A as defined above remains constant. However, the value of B^2 grows with time (until equilibrium is reached) due to compression and stretching of magnetic field lines (see Padoan & Nordlund 1999). If we define the Alfvén velocity using the rms value of the magnetic field strength, instead of its volume average, then the typical Alfvénic Mach number in our super–Alfvénic runs is $M_A \approx 2$, because of the formation of regions with large value of magnetic field strength (mainly dense regions, as found in observations).

The sonic Mach number of observed turbulent motions in molecular clouds is $M_S > 10$ on the scale of several parsecs, and decreases toward smaller scale. The turbulent velocity becomes comparable to the speed of sound only on very small scale, ≤ 0.1 pc. In order to study the effect of the sonic Mach number on the SCF, we have computed MHD models with different values of M_S, $M_S = 10$, 5, 2.5, 1.25 and 0.625. Each model has been run for approximately six dynamical times (the dynamical time is here defined as the ratio of half the size of the computational box and the rms flow velocity), in order to achieve a statistically relaxed state, independent of the initial conditions.

The velocity and density fields from the final snapshot of each model have been used to compute ^{13}CO $J = 1 - 0$ spectra, solving the radiative transfer with a non–LTE Monte Carlo code (§ 4.2). While the MHD calculations are independent of the physical value of the average gas density, the size of the computational mesh (or the column density) and the kinetic temperature, these physical parameters are necessary inputs for the radiative transfer calculations.

The models are scaled to physical units assuming a value for i) the kinetic temperature,

$T_{\rm K}$, that determines the physical unit of velocity (the numerical unit of velocity is the speed of sound); ii) the average gas density, $\langle n \rangle$; iii) the size of the computational box, L_0. For all models we have assumed $T_{\rm K} = 10$ K, typical of molecular clouds. The dependence of average gas density and cloud size on the rms turbulent velocity (or sonic Mach number, assuming a constant value of $T_{\rm K}$) is well–approximated by empirical Larson type relations (Larson 1981). However, the size–velocity relation has a large intrinsic scatter (e.g. Falgarone, Puget & Perault 1992), and the density–size relation has been criticized by several authors (e.g. Vazquez-Semadeni, Ballesteros-Paredes & Rodriguez 1997). For these reasons, we scale the MHD models in four different ways. These four sets of models are all based on the same five MHD turbulence models and differ from each other only in the way they are rescaled to physical units when computing the radiative transfer. Models A1 to A5 and B1 to B5 have all the same value of the average density, $\langle n \rangle = 300$ cm^{-3}. Models A1 to A5 have all the same size $L_0 = 5$ pc and column density $N_{\rm col} = 4.5 \times 10^{21}$ cm^{-2}; models B1 to B5 have $L_0 = 20$ pc and $N_{col} = 1.8 \times 10^{22}$ cm^{-2}. Models A1R to A5R and B1R to B5R are rescaled using the Larson type relations:

$$M_{\rm S} = M_{\rm S,1pc} \left(\frac{L}{1pc} \right)^{0.5} \tag{6}$$

where a temperature $T = 10$ K is assumed, and

$$\langle n \rangle = n_{\rm 1pc} \left(\frac{L}{1pc} \right)^{-1} \tag{7}$$

that is equivalent to a constant mean surface density. Models A1R to A5R have the same column density as models A1 to A5, that is $n_{\rm 1pc} = 1.5 \times 10^3$ cm^{-3} in equation (7); they also have sizes L_0 =10, 2.5, 0.625, 0.156 and 0.039 pc respectively, which implies $M_{\rm S,1pc} = 3.16$ in equation (6). Models B1R to B2R have the same column density as models B1 to B5, that is $n_{\rm 1pc} = 6.0 \times 10^3$ cm^{-3} in equation (7); they have sizes L_0 =20, 5, 1.25, 0.31 and 0.078 pc respectively, which implies $M_{\rm S,1pc} = 2.23$ in equation (6). Finally, the equipartition model (model E) has been computed only for one value of the rms sonic Mach number,

$M_S = 10$. It is rescaled to the Larson type relations only once, for a size of 10 pc and a column density of $N_{col} = 4.5 \times 10^{21}$ cm^{-2}. For this model we have computed spectral maps along 5 different directions, three orthogonal to the faces of the numerical mesh, as in the other experiments, and two along diagonal directions.

In order to test the ability of the SCF to rule out unphysical models, we have also computed two stochastic models, S2 and S4. In both models the density field is a random field with a Log–Normal probability distribution function, and a power law power spectrum with power law exponent equal to -1 (the approximate value found in our MHD models). The velocity field is generated as a Gaussian field, also with power law power spectrum. The power law exponent of the velocity field power spectrum is -2 (close to the actual value in the MHD models) in model S2 and -4 in model S4. For the purpose of computing the radiative transfer and the synthetic spectral maps, both models have been scaled to a physical size $L_0 = 20$ pc and a column density $N_{col} = 4.5 \times 10^{21}$ cm^{-2}.

These two stochastic models are unphysical in the sense that they are not solutions of the fluid equations. Statistical properties such as the power spectrum and the probability density function of density and velocity may be similar to those of flows obtained by solving the fluid equations, but their phase correlations are unphysical. This is in part illustrated by the fact that these stochastic models look clumpy, rather than filamentary as real clouds and MHD models. Furthermore, their velocity and density fields cannot be self–consistent because they are computed independently of each other. It is shown below that the SCF method can indeed rule out these unphysical models.

The sonic rms Mach number, M_S, the average gas density, $\langle n \rangle$, and the physical size, L_0, of the different models used for the radiative transfer computations are given in Table 3.

4.2. Radiative Transfer and Synthetic Spectral Maps

The radiative transfer calculations were carried out with a Monte Carlo program which is a generalization of the one-dimensional Monte Carlo method (Bernes 1979) into three dimensions. The model cloud is divided into small, cubic cells in which physical properties are assumed to be constant. The discretization allows the inclusion of arbitrary kinetic temperature and molecular abundance variations. However, in the present calculations, the temperature and relative abundances are kept constant. The 2.73 K cosmic background is used as the external radiation field. There are important differences between our program and the normal Monte Carlo method, and some principles of the implementation are given below. A detailed description is given elsewhere (Juvela 1997).

In the basic Monte Carlo method radiation field is simulated with photon packages, each representing a number of real photons. The packages are created at random velocities at random locations and sent toward random directions. Each package is followed through the cloud and interactions between photons and molecules are counted. Later this information is used to solve new estimates for the level populations of the molecules. In our method the radiative transfer is simulated along random lines going through the cloud. Initially, as a photon package enters the cloud it contains only background photons. As the package goes through a cell in the cloud some photons emitted by this cell are added to the package and, in particular, the number of photons absorbed within the emitting cell is calculated explicitly. This becomes important when cells are optically thick and, compared with normal Monte Carlo simulation, ensures more accurate estimation of the energy transfer between cells. In our program each simulated photon package represents intensity of all simulated transitions and Doppler shifts at the same time. The number of individual photon packages is correspondingly smaller, and in the present case we use 240 000 photon packages per iteration. The lines are divided into 70 fixed velocity channels. There is no

noise associated with random sampling of Doppler shifts. The simulated velocity range was adjusted according to the velocity range found in the model clouds. The channels are narrow compared with the total line widths and less or equal to the smallest intrinsic line widths in the cells. The velocity discretization is therefore not expected to affect the results of the calculations.

On each iteration new level populations are solved from the equilibrium equations and iterations are stopped when the relative change is below $\sim 2.0 \cdot 10^{-4}$ in all cells. Only six lowest levels were tested for convergence. The relative changes tend to be largest on the upper levels where the level populations become very small and, on the average, the convergence of the relevant first energy levels is much better than the quoted limit. The total number of energy levels included in the calculations was nine, a number clearly sufficient in case of excitation temperatures below 10 K. The collisional coefficients were taken from Flower & Launay (1985) and Green & Thaddeus (1976).

The final level populations were used to calculate maps of 90×90 spectra toward three directions perpendicular to the faces of the MHD data cube. For the equipartition model E spectra were calculated also along two diagonal directions. In these cases the maps of 90×90 spectra do not extend over the whole projected cloud area. Each spectrum corresponds to the intensity calculated along one line of sight i.e. they are not convolved with a larger beam. The spectra contain 60 velocity channels as in the Monte Carlo simulation. The results were compared with spectra calculated assuming LTE conditions. The comparison showed that for typical physical conditions found in molecular clouds the LTE assumption would be unsuitable (Padoan et al. 1998).

5. Observational Correlations and Theoretical Models

Most observational and theoretical spectral maps yield a SCF that can be approximated by a single power law within a range of spatial separations, often spanning over an order of magnitude. From each power law fit we compute its slope, α, and its value at 1 pc, $S_0(1\mathrm{pc})$. We also compute the value of the velocity dispersion, σ_v, from each map, measured as the standard deviation of the ^{13}CO $J = 1 - 0$ spectrum averaged over the entire map. The values of α, $S_0(1\mathrm{pc})$ and σ_v computed from the observational maps are given in Table 2, while the values of the same quantities from the theoretical models are given in Table 3.

Every model provides three sets of values, because spectral maps have been computed using three orthogonal directions for the line of sight. Each group of three sets of values can be interpreted as the same model cloud being "observed" from different directions, or as three different model clouds with comparable rms velocity. In the equipartition model, E, the rms velocities inferred from different directions are very different from each other, the largest rms velocity being found in the direction parallel to the mean magnetic field (along the z axis), and the lowest in the directions perpendicular to the magnetic field. For this model we have also computed spectral maps from two more lines of sight, corresponding to diagonal directions across the computational box.

Figure 4 shows the SCF of the model A1R, with line of sight parallel to the direction of the mean magnetic field. The SCF of the equipartition model E is also shown for four lines of sight, two diagonal, one parallel to the direction of the mean magnetic field and one parallel to it. The figure shows that the SCF of model E is very sensitive to the line of sight, due to the large variations of the rms velocity in different directions relative to the mean magnetic field.

The velocity dispersion relative to the speed of sound, or the value of the sonic Mach number, is the most important physical parameter characterizing the nature of the

turbulence. We therefore study the dependence of the SCF on the turbulent velocity dispersion (or the rms sonic Mach number, $M_{\rm S}$) and below propose to use this dependence to test theoretical models against the observational data.

In Figure 5 the slope of the SCF is plotted against the line of sight velocity dispersion. The top panels show the models of constant size and constant average gas density (models A1 to A5 -left, and B1 to B5 -right); the bottom panels show the models rescaled according to Larson type relations (models A1R to A5R -left and B1R to B5R -right). The observations indicate a strong correlation between α and σ_v, over an order of magnitude in σ_v. The growth of the absolute value of α with increasing σ_v can be expressed with the following least square fit to the observational data:

$$\alpha_{\rm obs} = 0.30\,\sigma_{v,{\rm obs}}^{0.37} \tag{8}$$

Least square fits have been computed also for the super–Alfvénic MHD models, using only results from the super–sonic runs ($\sigma_v > 0.2$ km/s). The runs with sonic Mach number $M_{\rm S} = 1.25$ and $M_{\rm S} = 0.62$ are not included in the least square fits because they do not seem to follow the same power laws and because our sample does not include any observational map with $\sigma_v < 0.2$ km/s. The least square fit for the super–sonic and super–Alfvénic models rescaled with Larson type relations (A1R to A3R) is:

$$\alpha_{\rm MHD} = 0.30\,\sigma_{v,{\rm MHD}}^{0.40} \tag{9}$$

that is practically indistinguishable from the observational result. The corresponding models not scaled with the Larson type relations (A1 to A3) do not match the observational results as well as models A1R to A3R (see Figure 5 top left panel). Even worse is the case of models of type B (right panels of Figure 5), which shows that the observational results can rule out models with column density a few times larger than typical. The stochastic models S2 and S4 are indistinguishable from each other; they are also totally inconsistent

with the empirical α–σ_v relation, which allows them to be ruled out as invalid by the SCF method. Finally, the equipartition model E provides values that are consistent with the observations, and comparable to the super–Alfvénic models, apart from a larger scatter of values between different lines of sight.

The value of $S_0(1\mathrm{pc})$ is plotted against σ_v in Figure 6. The top panels show the models of constant size and the bottom panels the models scaled with the Larson type relations, as in Figure 5. The values of $S_0(1\mathrm{pc})$ and σ_v from the observational maps are weakly correlated, with $S_0(1\mathrm{pc})$ slightly increasing with increasing σ_v:

$$S_{0,\mathrm{obs}}(1\mathrm{pc}) = 0.45\,\sigma_{v,\mathrm{obs}}^{0.13} \tag{10}$$

A tight correlation is instead found in the models of constant size (top panels of Figure 6), with $S_0(1\mathrm{pc})$ decreasing with increasing σ_v. This inconsistency between the models and the observations is most likely due to the fact that molecular clouds of 5 to 20 pc of size (as assumed by these models) are never found with velocity dispersion as low as assumed by the least turbulent of the constant size models. The bottom panels of Figure 6 show that the inconsistency is in fact mostly resolved as soon as the model sizes are scaled according to the Larson type relation. For the models A1L to A3L we obtain:

$$S_{0,\mathrm{MHD}}(1\mathrm{pc}) = 0.40\,\sigma_{v,\mathrm{MHD}}^{0.07} \tag{11}$$

The equipartition model yields values of $S_0(1\mathrm{pc})$ and σ_v consistent with the observations in all directions, but the one parallel to the mean magnetic field. It could be concluded that either none of the observed objects has a significant component of the magnetic field along the line of sight, or that all of them have a magnetic field weaker than predicted by the equipartition model, consistent with the super–Alfvénic models.

In Figure 7 we have plotted observations and models on the α–$S_0(1\mathrm{pc})$ plane. The constant size models are again inconsistent with the observations, as is expected since the

observational maps span a large range of scales. When the models are scaled according with the Larson type relations and the realistic average column density of 4.5×10^{21} cm^{-2} (Myers & Goodman 1988), the observed scatter in the α–S_0(1pc) plane is reproduced. The trend of the absolute value of α to increase with S_0(1pc) for large values of both of them is also reproduced, between models with rms Mach 5 and 10 (A2R and A1R respectively); however, models with rms Mach of 20 or 30 would be necessary to fit the α and S_0(1pc) values measured for the Rosette molecular cloud, which can be appropriately resolved only with a numerical resolution in excess of 256^3 computational cells.

While the stochastic models S2 and S4 are only marginally inconsistent with the observations in this plot, the line of sight parallel to the direction of the mean magnetic field in the equipartition model E is again totally inconsistent with the observational data (as if the linear size of the model was far too small for that particular component of the velocity dispersion).

6. Discussion

The SCF has been proposed as a statistical tool to test the validity of theoretical models describing the structure and dynamics of star forming clouds (Rosolowsky et al. 1999). In a previous work we improved the SCF method by studying its dependence on spatial and velocity resolution and on instrumental noise (Padoan, Rosolowsky & Goodman 2001). Here we have applied that improved SCF to a number of large ^{13}CO maps of molecular cloud complexes and obtained empirical correlations that can be used to test theoretical models. Of the theoretical models we have computed some compare well with the empirical correlations and some do not, which shows that the SCF can be used as an effective tool to rule out inappropriate or unphysical models.

The empirical correlations we have obtained relate the values of α, $S_0(1\mathrm{pc})$ and σ_v with each other. The α–σ_v correlation rules out the unphysical stochastic models (S2 and S4). Such models were found to produce spectral line profiles similar to observational ones by Dubinski, Narayan & Phillips (1995). They have also been used as models of the density field in molecular clouds by Stutzki et al. (1998) and to calibrate their principal component analysis by Brunt & Heyer (2002). The SCF α–σ_v correlation shows that stochastic models are inappropriate to describe the structure of molecular cloud complexes.

The $S_0(1\mathrm{pc})$–σ_v and the α–$S_0(1\mathrm{pc})$ correlations do not favor the model with equipartition of kinetic and magnetic energies (model E). Such model yields too small values of $S_0(1\mathrm{pc})$ compared with the observational data, when seen in the direction parallel to the average magnetic field. This means either that none of the many observed regions has an average magnetic field oriented close to the direction of the line of sight or that all the observed regions have an average magnetic field strength smaller than in the equipartition model, and consistent with super–Alfvénic conditions. The second interpretation is favored by recent results showing that the dynamics of molecular clouds on large scales is consistent with super–Alfvénic turbulence and inconsistent with the equipartition model (Padoan & Nordlund 1997, 1999). This is also confirmed by the fact that the super–Alfvénic models rescaled with Larson type relations reproduce the empirical SCF correlations. However, the total number of truly independent directions on the sky in the present observational sample is still too small to rule out the equipartition model based on the SCF results.

Models not scaled with Larson type relations (A1–A5, B1–B5) and models with larger–than–average column density (B1–B5, B1R–B5R) have also been compared with the empirical SCF correlations to show that incorrectly scaled models are readily ruled out by the SCF method.

The comparison between our theoretical models and the observational data could be

improved if more objects with sub–sonic turbulence were available in the observational sample. Small velocity dispersion is found in small objects, according to Larson's velocity–size relation, or to the power spectrum of turbulence. The spatial resolution in single dish surveys is typically too low to sample a small object (fraction of a parsec) with a very large spectral maps (several thousands of spectra). The only exceptions in the observational sample used in this work are L1512 and L134a. These two large maps of nearby clouds with very low velocity dispersion were obtained by Falgarone et al. (1998) as part of their IRAM key project, focused on regions of relatively low column density at the edges of molecular cloud complexes.

Maps of large regions with very large velocity dispersion are instead more easily obtained from observations than in numerical simulations. Assuming a gas kinetic temperature of the order of 10 K, a line of sight (one dimensional) velocity dispersion in excess of 2 km/s corresponds to a sonic rms Mach number of the flow $M_S \geq 20$. In the present work we have not computed numerical flows with $M_S > 10$, since that would require a larger numerical resolution (the density contrast grows with the value of M_S). For this reason the models do not reach the largest values of σ_v, α and S_0(1pc) obtained from the observations (from the maps of the Rosette molecular cloud complex). The progression of models toward increasing values of M_S suggests that a model with $M_S \geq 20$ would likely fit the observed α–S_0(1pc) values found in the Rosette molecular cloud complex, where the observed velocity dispersion is in excess of 2 km/s. This is illustrated in Figure 8. The left panel of Figure 8 shows the α–S_0(1pc) for the observational data. The shaded area shows the range of values covered by the theoretical models A1R to A5R. The right panel shows the same plot for the model A1R to A5R. Each diagonal segment connects the values for the three directions of each model. The values of M_S and L_0 of the models are also given in the plot. The arrow marks the direction of increasing M_S suggesting that models with $M_S \approx 20$ may fit the observations with the largest velocity dispersion.

7. Summary and Conclusions

In the present work we have computed the spectral correlation function (SCF) of spectral maps of molecular cloud complexes and regions within them, observed in the J=1–0 transition of ^{13}CO. We have found that the SCF is a power law over approximately an order of magnitude in spatial separation. The power law slope of the SCF, α, its normalization, S_0(1pc), and the spectral line width averaged over the whole map, σ_v, have been computed for all the observational maps. We have obtained empirical correlations between these quantities and have proposed to use them to test the validity of theoretical models of molecular clouds.

Theoretical models of spectral line maps have been generated by computing the radiative transfer through the numerical solutions (density and velocity fields) of the magneto-hydrodynamic (MHD) equations, for turbulent flows with different values of the rms sonic and Alfvénic Mach numbers, and also through stochastic density and velocity fields with different power spectra. Super-Alfvénic MHD models rescaled according to Larson type relations are in the best agreement with the empirical correlations. Unphysical stochastic models are instead ruled out. MHD models with equipartition of magnetic and kinetic energy of turbulence do not reproduce the observational data when their average magnetic field is oriented approximately parallel to the line of sight. Finally, MHD models not rescaled according to Larson type relations are also inconsistent with the observational data.

We cannot exclude the possibility that different physical models for the dynamics of molecular clouds, or even unphysical models, that we have not tested here, would satisfy the empirical correlations found in this work. However, we have shown that the SCF method is able to rule out certain unphysical or incorrectly scaled models. Reproducing these SCF results should be considered as a necessary (but not sufficient) condition for the validity of

theoretical models describing the structure and the dynamics of molecular clouds. Models for which the SCF or similar statistical tests cannot be computed to allow a quantitative comparison with observed spectral maps cannot be legitimately evaluated.

The comparison between theory and observations presented in this work requires significant computational resources. Numerical simulations of three dimensional turbulent flows must be run at large resolution and the radiative transfer has to be computed in three dimensions in order to generate synthetic spectral maps of the observed molecular transitions. The type of models and the physical parameters investigated in this work are therefore limited to a few significant cases. Future work should investigate the SCF of a larger variety of models, including different magnetic field intensities and flows with gravitationally collapsing cores.

We are grateful to Eve Ostriker and Jim Stone for helpful comments on our model–data comparison. This work was supported by an NSF Galactic Astronomy grant to AG. The work of PP was partially performed while PP held a National Research Council Associateship Award at the Jet Propulsion Laboratory, California Institute of Technology.

References

Arce, H. . G., Goodman, A. A. 2001, ApJ, 554, 132

Bensch, F., Stutzki, J., Ossenkopf, V. 2001, A&A, 366, 636

Bernes, C. 1979, A&A, 73, 67

Blitz, L., Stark, A. A. 1986, ApJL, 300, L89

Blitz, L., Williams, J. P. 1997, ApJL, 488, L145

Brunt, C. M., Heyer, M. H. 2002, ApJ, 566, 276

Dubinski, J., Narayan, R., Phillips, T. G. 1995, ApJ, 448, 226

Falgarone, E., Lis, D. C., Phillips, T. G., Pouquet, A., Porter, D. H., Woodward, P. R. 1994, ApJ, 436, 728

Falgarone, E., Panis, J.-F., Heithausen, A., Perault, M., Stutzki, J., Puget, J.-L., Bensch, F. 1998, A&A, 331, 669

Falgarone, E., Puget, J. L., Pérault, M. 1992, A&A, 257, 715

Flower, D. R., J.M., L. 1985, MNRAS, 214, 271

Gill, A. G., Henriksen, R. N. 1990, ApJL, 365, L27

Green, S., Thaddeus, P. 1976, ApJ, 205, 766

Heyer, M. H., Schloerb, F. P. 1997, ApJ, 475, 173

Hobson, M. P. 1992, MNRAS, 256, 457

Houlahan, P., Scalo, J. 1992, ApJ, 393, 172

Juvela, M. 1997, A& A, 322, 943

Kim, S., Dopita, M. A., Staveley-Smith, L., Bessell, M. S. 1999, AJ, 118, 2797

Kim, S., Staveley-Smith, L., Dopita, M. A., Freeman, K. C., Sault, R. J., Kesteven, M. J., McConnell, D. 1998, ApJ, 503, 674

Kleiner, S. C., Dickman, R. L. 1985, ApJ, 295, 466

Kleiner, S. C., Dickman, R. L. 1987, ApJ, 312, 837

Langer, W. D., Wilson, R. W., Anderson, C. H. 1993, ApJ, 408, L45

Larson, R. B. 1981, MNRAS, 194, 809

Lazarian, A., Pogosyan, D., Vázquez-Semadeni, E., Pichardo, B. . 2001, ApJ, 555, 130

Lis, D. C., Pety, J., Phillips, T. G., Falgarone, E. 1996, ApJ, 463, 623

Mac Low, M.-M., Ossenkopf, V. 2000, A&A, 353, 339

Miesch, M. S., Bally, J. 1994, ApJ, 429, 645

Miesch, M. S., Scalo, J., Bally, J. 1999, ApJ, 524, 895

Miesch, M. S., Scalo, J. M. 1995, ApJ, 450, L27

Mizuno, A., Onishi, T., Yonekura, Y., Nagahama, T., Ogawa, H., Fukui, Y. 1995, ApJ, 445, L161

Myers, P. C., Goodman, A. A. 1988, ApJ, 329, 392

Ostriker, E. C., Stone, J. M., Gammie, C. F. 2001, ApJ, 546, 980

Padoan, P., Bally, J., Billawala, Y., Juvela, M., Nordlund, Å. 1999, ApJ, 525, 318

Padoan, P., Juvela, M., Bally, J., Nordlund, Å. 1998a, ApJ, in press

Padoan, P., Juvela, M., Bally, J., Nordlund, Å. 1998b, ApJ, 504, 300

Padoan, P., Rosolowsky, E. W., Goodman, A. A. 2001, ApJ, 547, 862

Rosolowsky, E, W., Goodman, A. A., Wilner, D. J., Williams, J. P. 1999, ApJ, 524, 887

Scalo, J. M. 1984, ApJ, 277, 556

Stutzki, J., Bensch, F., Heithausen, A., Ossenkopf, V., Zielinsky, M. 1998, A&A, 336, 697

Stutzki, J., Güsten, R. 1990, ApJ, 356, 513

Vazquez-Semadeni, E., Ballesteros-Paredes, J., Rodriguez, L. F. 1997, ApJ, 474, 292

Williams, J. P., De Geus, E. J., Blitz, L. 1995, ApJ, 428, 693

This manuscript was prepared with the AAS LaTeX macros v4.0.

Figure captions:

Table 1 Main parameters of the observed spectral maps: Approximate size, distance, rms velocity over the whole map, telescope beam, spatial sampling, velocity channel width, average spectrum quality and bibliographic reference.

Table 2 Spectral line width averaged over the whole map, σ_v, power law slope of the SCF, α and SCF normalization, S_0(1pc), galactic longitude, l, and galactic latitude, b, for all the observed maps and selected regions within them.

Table 3 First three columns from the left: Model name, rms sonic Mach number of the flow and physical size of the computational mesh. Following columns: Line of sight velocity dispersion, SCF slope and SCF normalization, repeated for the three orthogonal directions for which synthetic spectral maps have been computed in each model. Values for the diagonal directions of model E are not given (they are within the ranges of values covered by the other three directions parallel and perpendicular to the mean magnetic field).

Figure 1: Top panel: Velocity integrated intensity map of the Perseus molecular cloud complex in the J=1-0 transition of ^{13}CO (Padoan et al. 1999) Bottom panel: Same as top panel, but for the Taurus molecular cloud complex (Mizuno et al. 1995). Smaller regions within the maps where the SCF has also been computed are highlighted.

Figure 2: Same as in Figure 1, but for the Rosette molecular cloud complex. Top panel from Heyer et al. (2001); bottom panel from Blitz & Stark (1986).

Figure 3: Top left panel: The SCF averaged over the entire map of the Perseus, Rosette and Taurus molecular cloud complexes. Solid lines are least square fits to the power law sections of the SCF. The exponents α of the power law fits are also given in the figure. Top right panel: SCF of the whole map of the Perseus molecular cloud complex and of smaller regions within the same map. Bottom left panel: SCF of the Taurus molecular cloud complex and of smaller regions within the same map. Bottom right panel: SCF of PVCeph and HH300.

Figure 4: The SCF computed from MHD models. Asterisk symbols are for the super-Alfvénic model A1R in the Z direction (parallel to the mean magnetic field). Diamond symbols are for the equipartition model in the X and Z direction (perpendicular and parallel to the average magnetic field direction respectively) and along two diagonal directions ($D1$ and $D2$). The slope of the SCF increases with increasing rms velocity. The SCF is therefore weakly dependent on the direction of the line of sight for the super-Alfvénic model, while it is much steeper in the direction parallel to the magnetic field (larger rms velocity) than in the perpendicular direction in the equipartition model.

Figure 5: SCF slope versus velocity dispersion. The top panels show the models of constant size and constant average gas density as asterisks (models A1 to A5 –left, B1 to B5 –right); the bottom panels show the models rescaled according to Larson type relations as asterisks (models A1R to A5R –left, B1R to B5R –right). Observational values are shown by square symbols, the equipartition model with plus symbols and the stochastic models as diamonds.

Figure 6: SCF value at 1 pc versus velocity dispersion. Different panels show different models as in Figure 5. Symbols are also as in Figure 5.

Figure 7: SCF slope versus SCF value at 1 pc. Symbols and panels as in Figure 5.

Figure 8: Top panel: Values of α and $S_0(1\mathrm{pc})$ from the observations. Some of the symbols are labeled with the region name. The shaded area shows the range of values covered by the models A1R to A5R. Bottom panel: Same shaded area as in the left panel. Diagonal segments shows the range of values of α and $S_0(1\mathrm{pc})$ for the three directions of each model. The rms sonic Mach number of the corresponding model is given on the right hand side of each segment, while the value of the linear size is given on the left hand side. The arrow indicates the progression of models toward larger values of sonic Mach number, M_{S}.

MC	L [pc]	D [Kpc]	σ_v [km/s]	Beam [pc]	dx [pc]	dv [km/s]	$\langle Q \rangle$	reference
Taurus	30	0.14	0.97	0.11	0.081	0.10	2.3	Mizuno et al. 1995
Perseus	30	0.30	2.01	0.16	0.087	0.27	2.8	Padoan et al. 1999
Rosette	45	1.60	2.45	0.84	0.70	0.68	2.1	Blitz & Stark 1986
Rosette	35	1.60	1.86	0.36	0.23	0.06	3.8	Heyer et al. 2001
L1524	1.5	0.14	0.79	0.032	0.015	0.10	5.2	Bensch 2002
Polaris	1.5	0.11	0.70	0.025	0.012	0.10	1.3	Bensch et al. 2001
HH300	2	0.14	1.24	0.032	0.023	0.022	1.5	Arce & Goodman 2(
PVCeph	3	0.50	0.98	0.114	0.083	0.022	1.8	Arce & Goodman 2(
Polaris	0.3	0.11	0.53	0.012	0.004	0.052	6.3	Falgarone et al. 199
L1512	0.3	0.15	0.20	0.016	0.005	0.052	11.7	Falgarone et al. 199
L134a	0.3	0.15	0.24	0.016	0.005	0.052	13.3	Falgarone et al. 199

Table 1:

Region	σ_v [km/s]	α	$S_0(1pc)$	l	b
Taurus	0.97	0.24	0.47	170.8	-16.2
T1	0.71	0.27	0.46	174.5	-13.8
T2	0.85	0.26	0.48	168.0	-16.1
T3	0.53	0.25	0.46	166.3	-16.8
T4	0.96	0.32	0.41	169.8	-16.1
T5	0.99	0.31	0.41	170.8	-17.0
T6	0.85	0.30	0.40	174.2	-16.3
T7	0.42	0.27	0.46	166.2	-17.3
Perseus	2.01	0.32	0.42	160.0	-19.3
P1 (B5)	1.20	0.29	0.51	161.2	-16.8
P2	1.33	0.30	0.44	160.7	-18.8
P3 (B1)	1.03	0.27	0.45	159.8	-20.1
P4 (NGC1333)	1.33	0.34	0.53	158.8	-20.5
P5 (L1448)	1.53	0.29	0.51	158.6	-21.6
Rosette (Bell Lab)	2.45	0.50	0.65	207.5	-1.8
R1B	2.18	0.42	0.60	207.3	-1.8
Rosette (FCRAO)	1.86	0.39	0.52	207.3	-1.8
R1	1.40	0.38	0.45	207.5	-1.8
R2	0.86	0.36	0.50	206.9	-1.8
L1524	0.79	0.23	0.44	173.3	-16.3
Polaris (FCRAO)	0.70	0.27	0.32	123.4	24.9
HH300	1.24	0.30	0.35	172.9	-16.7
PVCeph	0.98	0.32	0.39	102.9	15.2
Polaris (IRAM)	0.54	0.27	0.26	123.7	24.9
L1512	0.20	0.18	0.39	171.8	-5.2
L134a	0.24	0.13	0.49	4.3	35.8

Table 2:

			x			y			z		
Model	M_S	L_0 [pc]	σ_v [km/s]	α	S_0(1pc)	σ_v [km/s]	α	S_0(1pc)	σ_v [km/s]	α	S_0
MHD Models ($\langle n \rangle = 300$ cm^{-3})											
A1	10.0	5	1.13	0.30	0.37	1.36	0.32	0.34	1.24	0.35	0
A2	5.0	5	0.56	0.25	0.46	0.71	0.30	0.39	0.67	0.28	0
A3	2.5	5	0.30	0.19	0.55	0.38	0.24	0.48	0.36	0.21	0
A4	1.2	5	0.17	0.13	0.66	0.17	0.15	0.64	0.18	0.16	0
A5	0.6	5	0.12	0.13	0.68	0.11	0.10	0.71	0.12	0.14	0
B1	10.0	20	1.21	0.26	0.64	1.42	0.27	0.61	1.33	0.27	0
B2	5.0	20	0.61	0.22	0.70	0.77	0.26	0.65	0.72	0.24	0
B3	2.5	20	0.33	0.18	0.73	0.41	0.23	0.68	0.39	0.20	0
B4	1.2	20	0.18	0.14	0.77	0.19	0.15	0.77	0.21	0.17	0
B5	0.6	20	0.13	0.13	0.79	0.13	0.11	0.81	0.14	0.14	0
Rescaled MHD Models ($\langle n \rangle = 6 \times 10^3$ cm^{-3} $L_{0,pc}^{-1}$)											
A1R	10.0	10	1.13	0.30	0.44	1.36	0.32	0.42	1.23	0.35	0
A2R	5.0	2.5	0.56	0.23	0.41	0.72	0.30	0.32	0.66	0.26	0
A3R	2.5	0.62	0.30	0.18	0.41	0.37	0.21	0.34	0.35	0.20	0
A4R	1.2	0.16	0.16	0.12	0.45	0.15	0.13	0.42	0.17	0.15	0
A5R	0.6	0.04	0.10	0.11	0.41	0.10	0.08	0.49	0.11	0.12	0
B1R	10.0	20	1.21	0.26	0.64	1.42	0.27	0.61	1.33	0.27	0
B2R	5.0	5	0.60	0.22	0.55	0.76	0.23	0.49	0.69	0.20	0
B3R	2.5	1.25	0.33	0.15	0.52	0.40	0.18	0.45	0.37	0.16	0
B4R	1.2	0.31	0.18	0.12	0.50	0.18	0.13	0.47	0.19	0.14	0
B5R	0.6	0.08	0.12	0.10	0.46	0.12	0.09	0.52	0.13	0.12	0
Equipartition MHD Model											
E	10.0	5	0.73	0.21	0.46	0.81	0.25	0.43	1.90	0.49	0
Stochastic Models											
S2	10.0	20	1.37	0.15	0.52	1.29	0.15	0.53	1.31	0.14	0
S4	10.0	20	1.23	0.16	0.47	1.17	0.15	0.49	1.17	0.17	0

Table 3:

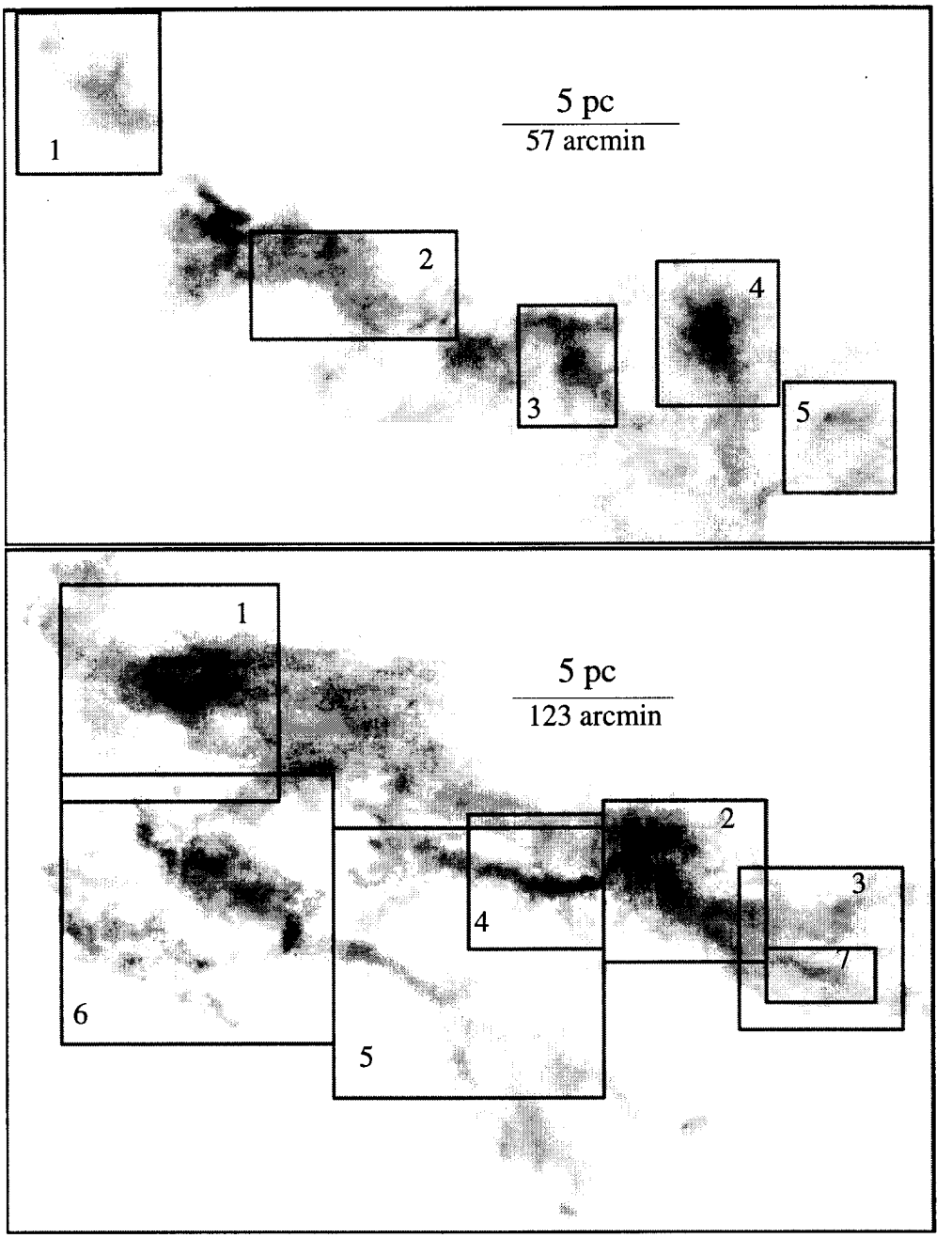

Fig. 1.—

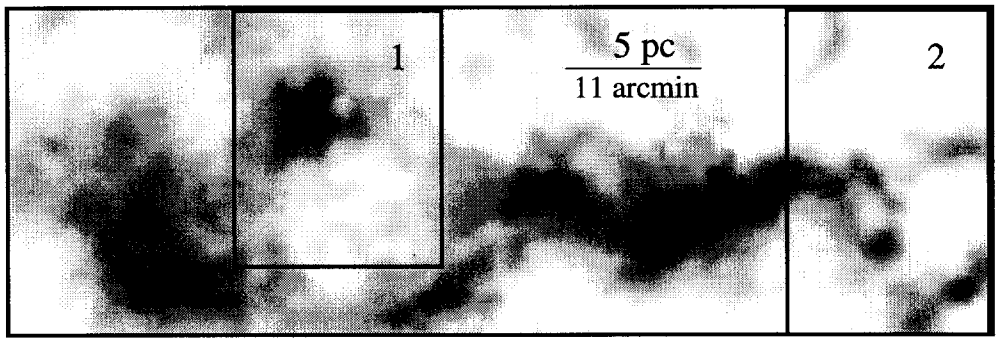

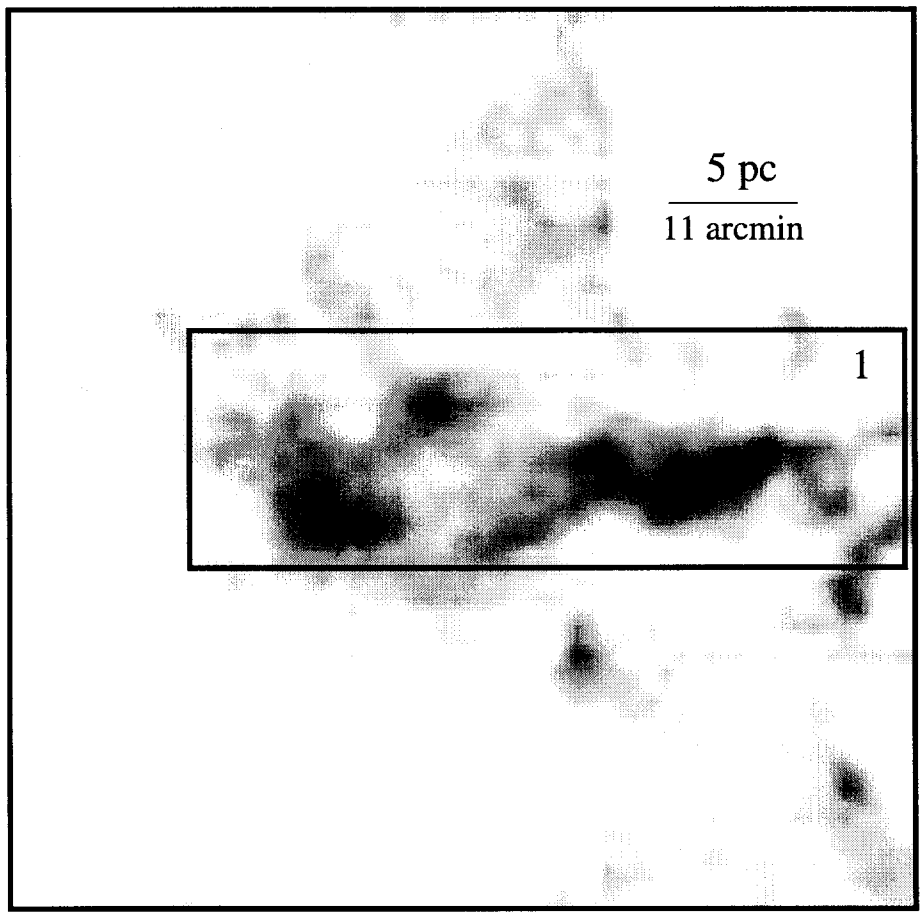

Fig. 2.—

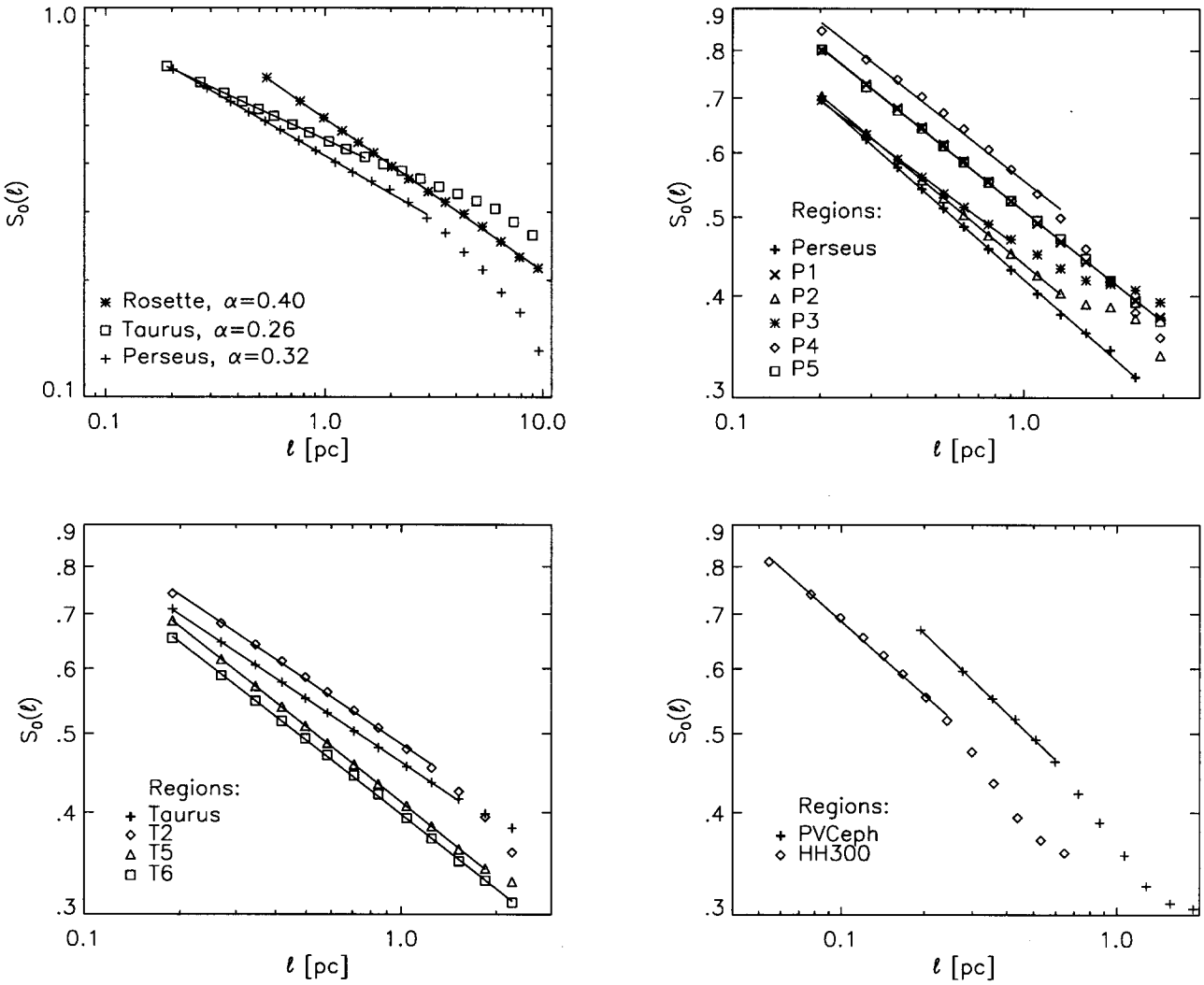
1.0
0.1
$S_0(\ell)$
0.1
1.0
10.0
ℓ [pc]
Rosette, α=0.40
Taurus, α=0.26
Perseus, α=0.32
.9
.8
.7
.6
.5
.4
.3
Regions:
Perseus
P1
P2
P3
P4
P5
Regions:
Taurus
T2
T5
T6
Regions:
PVCeph
HH300

Fig. 3.—

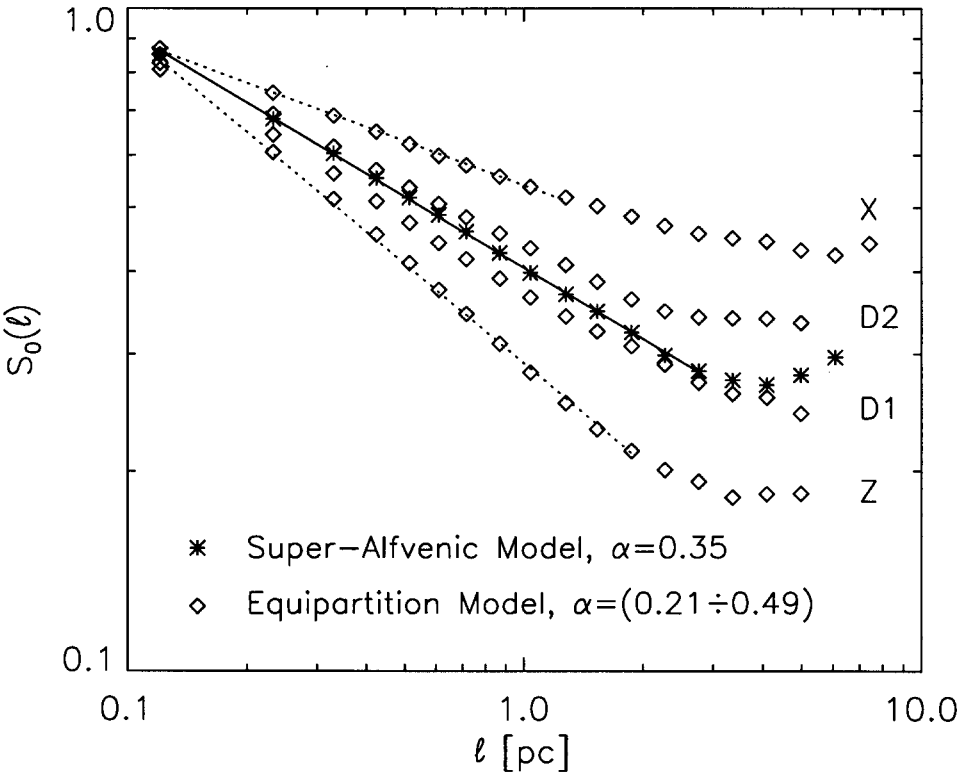
1.0
0.1
0.1
1.0
10.0
$S_0(\ell)$
ℓ [pc]
X
D2
D1
Z
Super−Alfvenic Model, α=0.35
Equipartition Model, α=(0.21÷0.49)

Fig. 4.—

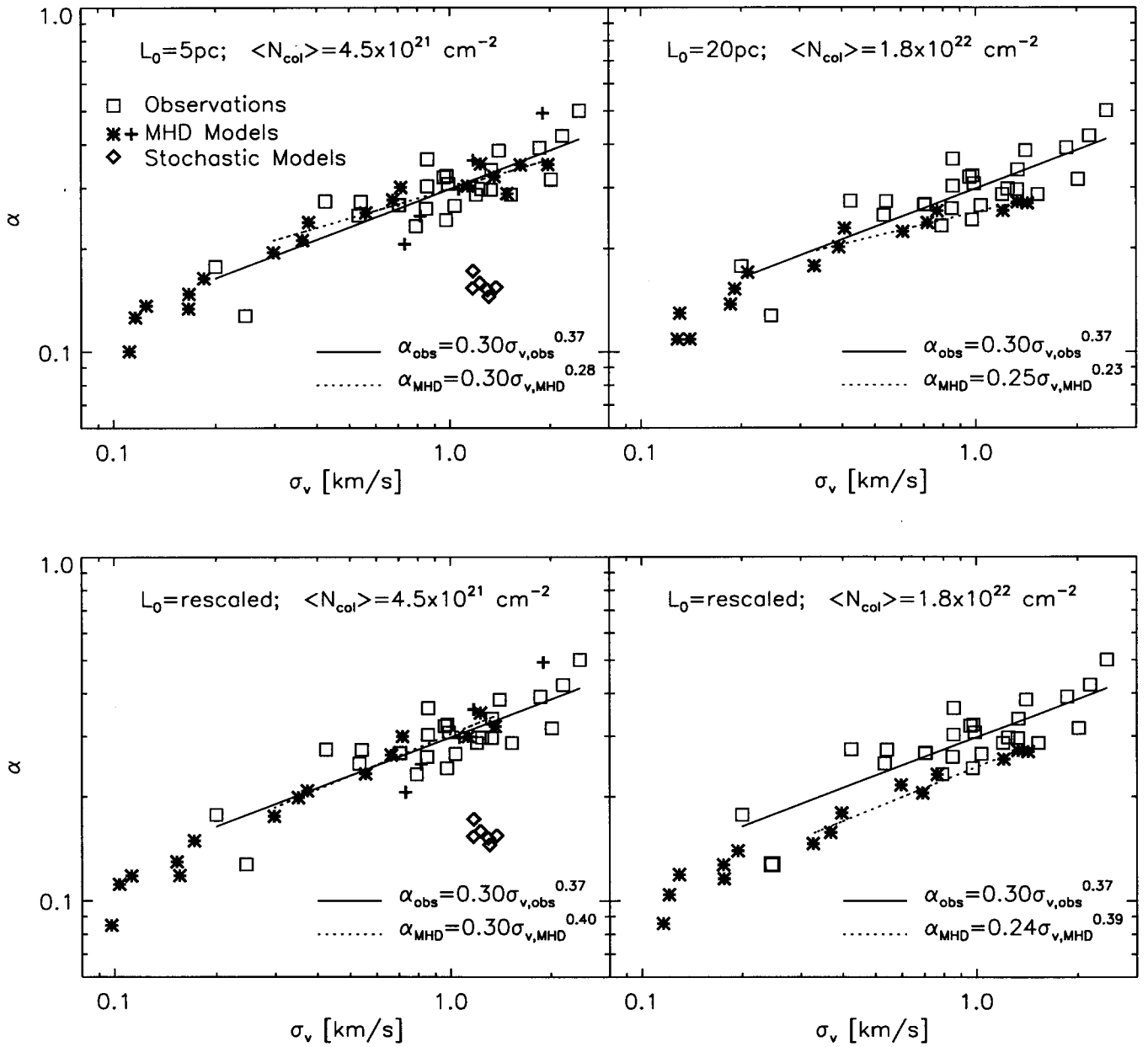
L0=5pc; <Ncol>=4.5x10^21 cm^-2
Observations
MHD Models
Stochastic Models
αobs=0.30σv,obs^0.37
αMHD=0.30σv,MHD^0.28
L0=20pc; <Ncol>=1.8x10^22 cm^-2
αobs=0.30σv,obs^0.37
αMHD=0.25σv,MHD^0.23
L0=rescaled; <Ncol>=4.5x10^21 cm^-2
αobs=0.30σv,obs^0.37
αMHD=0.30σv,MHD^0.40
L0=rescaled; <Ncol>=1.8x10^22 cm^-2
αobs=0.30σv,obs^0.37
αMHD=0.24σv,MHD^0.39
α
σv [km/s]
1.0
0.1

Fig. 5.—

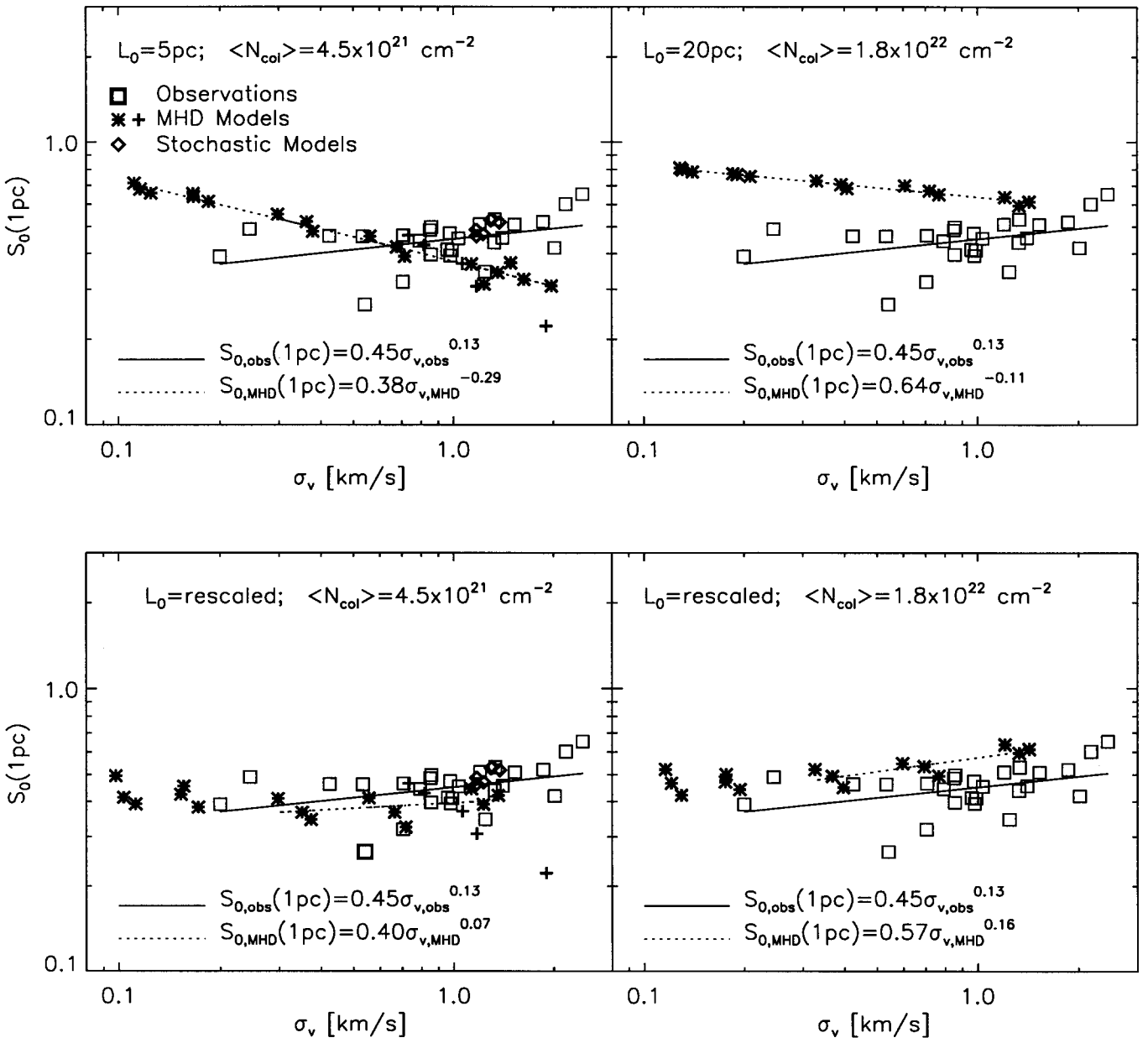
L0=5pc; <Ncol>=4.5x10^21 cm^-2
Observations
MHD Models
Stochastic Models
S0,obs(1pc)=0.45σv,obs^0.13
S0,MHD(1pc)=0.38σv,MHD^-0.29
L0=20pc; <Ncol>=1.8x10^22 cm^-2
S0,obs(1pc)=0.45σv,obs^0.13
S0,MHD(1pc)=0.64σv,MHD^-0.11
L0=rescaled; <Ncol>=4.5x10^21 cm^-2
S0,obs(1pc)=0.45σv,obs^0.13
S0,MHD(1pc)=0.40σv,MHD^0.07
L0=rescaled; <Ncol>=1.8x10^22 cm^-2
S0,obs(1pc)=0.45σv,obs^0.13
S0,MHD(1pc)=0.57σv,MHD^0.16
S0(1pc)
σv [km/s]
0.1
1.0

Fig. 6.—

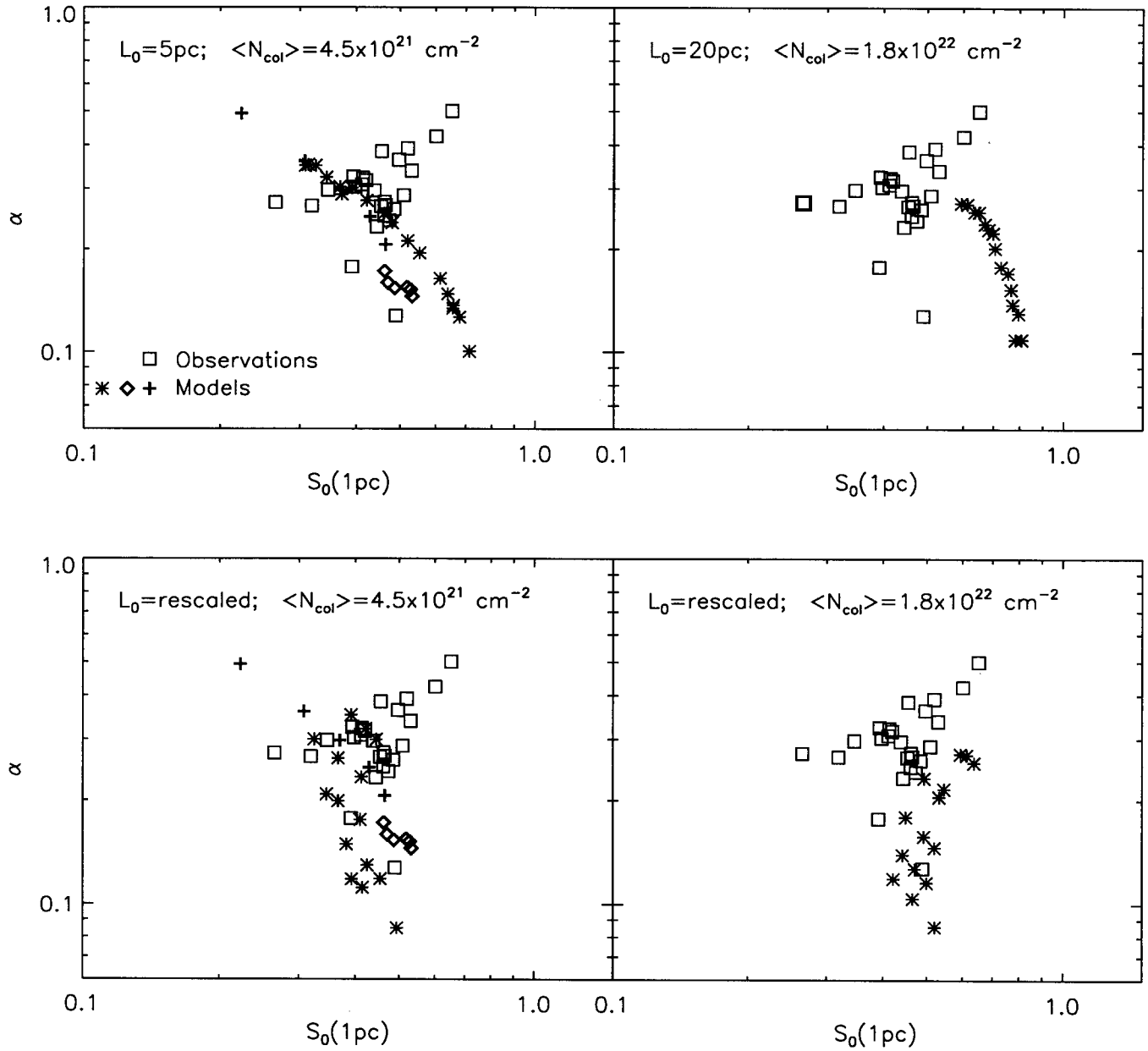
1.0
0.1
α
L0=5pc; <Ncol>=4.5x10^21 cm^-2
L0=20pc; <Ncol>=1.8x10^22 cm^-2
Observations
Models
0.1
1.0
S0(1pc)
L0=rescaled; <Ncol>=4.5x10^21 cm^-2
L0=rescaled; <Ncol>=1.8x10^22 cm^-2

Fig. 7.—

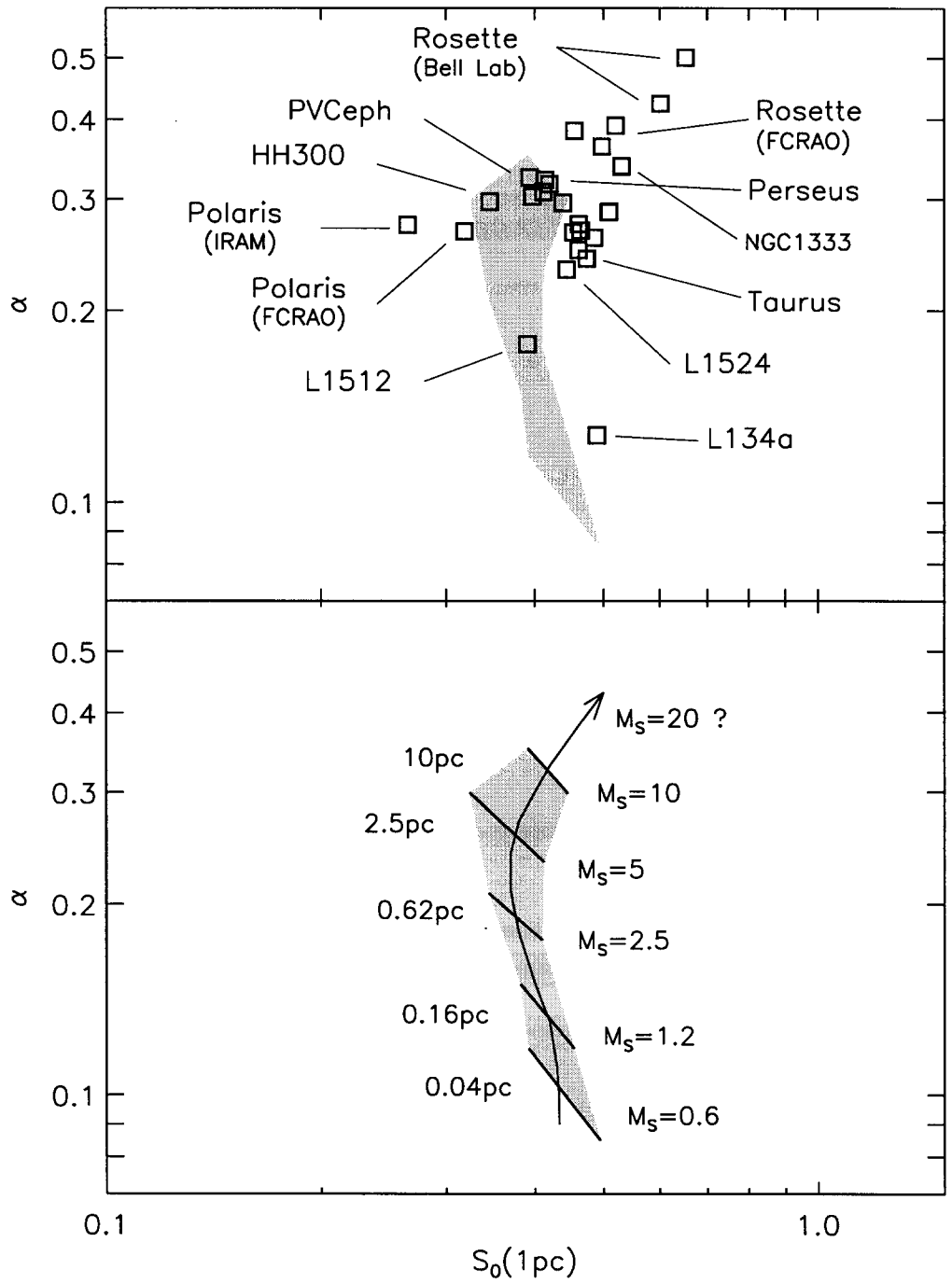
Rosette
(Bell Lab)
PVCeph
HH300
Polaris
(IRAM)
Polaris
(FCRAO)
L1512
Rosette
(FCRAO)
Perseus
NGC1333
Taurus
L1524
L134a
0.5
0.4
0.3
0.2
0.1
α
M_s=20 ?
10pc
M_s=10
2.5pc
M_s=5
0.62pc
M_s=2.5
0.16pc
M_s=1.2
0.04pc
M_s=0.6
0.1
1.0
S_0(1pc)

Fig. 8.—